Journal of Materials Chemistry B

ROYAL SOCIETY OF CHEMISTRY

PAPER

View Article Online
View Journal

Check for updates

Cite this: DOI: 10.1039/d6tb00003g

GalNAc-modified five-component lipid nanoparticles for liver-targeted delivery of p65 siRNA to alleviate cytokine storm in liver injury *via* NF-κB targeting

Zhijie Liang, †[ab] Shaorong Li,†[a] Huali Huang,[a] Shuying Luo,[a] Hongmian Jiang,[a] Lifeng Luo,[a] Jinzhuai Li *[c] and Kun Zhao*[d]

Acute liver injury (ALI) often triggers a systemic cytokine storm, in which the NF-κB subunit p65 plays a central role in driving inflammatory progression in hepatocytes. Delivering p65 siRNA to hepatocytes can effectively inhibit cellular inflammation and apoptosis. However, siRNA is inherently unstable and lacks tissue specificity. Lipid nanoparticles (LNPs) represent a mature delivery system with inherent liver tropism, yet their targeting efficiency remains suboptimal. To enhance hepatocyte-specific delivery, we developed a galactose-*N*-acetylgalactosamine (GalNAc)-modified five-component LNP (G-LNP) for liver-targeted delivery of p65 siRNA. GalNAc modification enables active targeting *via* asialoglycoprotein receptor (ASGPR)-mediated endocytosis, thereby improving hepatic accumulation and intracellular internalization. The optimized G-LNP formulation (1% DSPE–PEG2000–GalNAc) exhibited a particle size of 87 nm, a low PDI, and high encapsulation efficiency. *In vitro*, G-LNP–siP65 significantly enhanced transfection efficiency in AML-12 hepatocytes in an ASGPR-dependent manner, down-regulated p65 mRNA expression, alleviated CCl_4-induced oxidative stress (increased SOD and decreased MDA), and reduced pro-inflammatory cytokines (IL-6, TNF-α, and IL-1β). *In vivo* bioluminescence imaging confirmed superior and sustained liver accumulation of G-LNP–Luc compared to unmodified LNP. Furthermore, in a CCl_4-induced ALI mouse model, the G-LNP–siP65 treatment dramatically reduced serum ALT/AST levels, restored redox balance, and suppressed hepatic NF-κB expression, leading to marked amelioration of histopathological damage. Moreover, systemic safety evaluation demonstrated negligible hemolytic activity and a favorable hematological profile, as evidenced by reduced neutrophil percentage and decreased serum CRP levels. Collectively, GalNAc-modified five-component LNPs provide a potent and safe liver-targeted platform for p65 siRNA delivery, effectively mitigating cytokine storm and liver injury *via* NF-κB silencing. This strategy holds promise for nucleic acid-based therapies against acute and chronic liver diseases.

Received 1st January 2026,
Accepted 19th April 2026

DOI: 10.1039/d6tb00003g

rsc.li/materials-b

1 Introduction

When liver cells are damaged or undergo necrosis due to endogenous or exogenous factors such as viruses, drugs, alcohol, or ischemia, they release large amounts of damage-associated molecules (*e.g.*, ATP, DNA fragments, and mitochondrial components), which can trigger a cytokine storm. NF-κB serves as the core transcription factor linking liver injury signals with inflammatory responses.[1] Nearly all triggers (*e.g.*, DAMPs, pathogens, ROS, and TNF-α) activate NF-κB, inducing massive expression of pro-inflammatory factors like IL-1β, IL-6, and TNF-α.[2–4] These factors once released into the bloodstream further initiate cascade inflammatory reactions, ultimately leading to systemic immune storms.[5] Therefore, regulating NF-κB activity in target organs or tissues during early-stage acute inflammation and injury represents a critical therapeutic strategy. For instance, Ren *et al.* demonstrated that cumambrin B could inhibit overexpression of NF-κB in acute lung injury, thereby significantly reducing systemic inflammation and organ damage.[6] Additionally, compounds and formulations such as triptolide,[7] Shenghui decoction,[8] and naringin[9] have been shown to suppress inflammatory damage and

[a] *The Fifth Affiliated Hospital of Guangxi Medical University, Nanning 530000, China*
[b] *Research Institute of Lanzhou University in Shenzhen, Shenzhen 518000, China*
[c] *State Key Laboratory for the Chemistry and Molecular Engineering of Medicinal Resources, School of Chemistry and Pharmaceutical Sciences, Guangxi Normal University, Guilin 541004, China. E-mail: ljzmedicine@163.com*
[d] *Departments of Hepatobiliary Surgery, The First Affiliated Hospital of Guangxi Medical University, Nanning 530021, China. E-mail: kundoctor@163.com*
† These authors contributed equally to this work.

cytokine storms by inhibiting NF-κB expression or activity. In recent years, advances in nucleic acid drugs have enabled the targeted delivery of nucleic acids to specific cells in target organs, allowing for the modulation of particular proteins or genes. This approach offers a more precise therapeutic strategy that can circumvent the potential side effects of traditional drugs that act on multiple pathways.[10–12]

However, nucleic acid drugs themselves are inherently unstable, lack tissue targeting, and cannot passively enter cells. Drug delivery systems (DDSs) have thus become an indispensable component in nucleic acid drug therapy. Lipid Nanoparticles (LNPs) represent the most mature nucleic acid drug delivery system to date, with successful clinical applications including COVID-19 mRNA vaccines,[13] patisiran,[14,15] and NTLA-2001.[16] Moreover, an LNP inherently exhibits hepatic targeting properties. Combined with its efficient transfection capability, it holds significant potential value in treating acute and chronic liver diseases. After injection, Apolipoprotein E (ApoE) in the bloodstream adsorbs onto the LNP surface, specifically binding to liver cell LDLRs to trigger clathrin-mediated endocytosis.[17] Subsequently, ionizable lipids within LNPs undergo protonation in the acidic intracellular environment, causing membrane instability and rupture, thereby releasing the payload nucleic acids into the cytosol to exert their function. Nucleic acid therapies using LNPs as DDSs have demonstrated breakthrough efficacy in treating various liver diseases such as transsclerostatin amyloidosis and viral hepatitis.[18,19] However, current hepatic targeted delivery of LNPs primarily relies on passive mechanisms. By modifying LNPs through strategies such as galactose (Gal) ligand modification,[20] mannose modification,[21] and nucleoside modification,[22] the accumulation efficiency of LNPs in the liver can be enhanced, thereby improving therapeutic outcomes.

The asialoglycoprotein receptor (ASGPR), a C-type lectin receptor widely expressed on hepatocyte membranes, specifically binds galactose and its derivatives. By modifying LNPs with Gal ligands, receptor–ligand binding mediated by ASGPR-Gal with nanomolar affinity facilitates efficient intracellular transport of the ligand–receptor complex. This process demonstrates significantly higher internalization efficiency compared to passive targeting mechanisms,[23] thereby enhancing precision targeting to hepatocytes. Previous studies have shown that LNPs modified with Gal or its derivatives exhibit superior hepatocyte uptake rates compared to unmodified counterparts.[24,25] Notably, the uptake of modified LNPs was markedly reduced in the presence of ASGPR inhibitors, validating the functional efficacy of ASGPR-mediated endocytosis.[26,27] In terms of hepatic tissue targeting efficiency, the Gal-modified LNP demonstrates significant enrichment advantages. For instance, Zhang *et al.* found that LNPs modified with 2.5% galactose increased the delivery efficiency of luciferase mRNA in the liver by 61-fold.[28] Similarly, Liu *et al.* designed Gal-hyaluronic acid cationic solid lipid nanoparticles targeting both ASGPR and cluster of differentiation 44 (DC44) receptors, achieving substantial enhancement of drug absorption efficiency in hepatocytes.[29] GalNAc exhibits enhanced ASGPR binding capability due to the acetylation of its C2 hydroxyl group,[30,31] hepatocyte uptake efficiency of LNPs compared to galactose modification.[32] Several GalNAc-modified LNPs for nucleic acid delivery have entered clinical trials, including Givlaari for acute porphyria,[33] nedosiran for primary hyperoxaluria,[34] and hereditary transthyretin-mediated (hATTR) amyloidosis.[35] Structural modifications can further enhance the liver-targeting capability and therapeutic potential of GalNAc. For instance, triantenna GalNAc provides stronger ASGPR anchoring,[36] while GalNAc-PDS conjugation leverages synergistic effects of ASGPR recognition and PDS-mediated transmembrane transport to improve delivery efficiency.[29] These findings demonstrate the superior liver-targeting properties of GalNAc and reveal its potential for structural optimization and expanded therapeutic applications.

Leveraging these technological advancements, we developed a GalNAc-modified LNP delivery system for P65 siRNA targeting acute liver injury. By introducing the GalNAc ligand for ASGPR-mediated active targeting, this strategy significantly improves P65 siRNA delivery efficiency. It achieves rapid and precise suppression of NF-κB expression in hepatocytes, thereby blocking the NF-κB-driven inflammatory storm. This approach establishes a proof of concept for a novel therapeutic strategy for acute liver injury (Scheme 1).

2 Materials and methods

2.1 Main materials and reagents

All lipids, including the ionizable lipid DLin-MC3-DMA, 1,2-distearoyl-*sn-glycero*-3-phosphocholine (DSPC), cholesterol, and 1,2-dimyristoyl-*rac-glycero*-3-methoxypolyethylene glycol-2000 (DMG–PEG2000), were purchased from AVT Pharmaceutical Co., Ltd (Shanghai, China). The protected targeting ligand precursor, peracetylated GalNAc(tri)–OAc–PEG2000–DSPE, was obtained from Merro Biotech (Shanghai, China). P65 siRNA (sense: 5′ GCGACAAGGUGCAGAAAGA3′; antisense: 5′CGCUG UUCCACGUCUUUCU3′) was custom-synthesized by Sangon Biotech (Shanghai, China). Firefly luciferase (Luc) mRNA and the Luciferase Assay Kit were sourced from Vazyme Biotech (Nanjing, Jiangsu, China). D-Luciferin, potassium salt, was acquired from MedChemExpress (Monmouth Junction, NJ, USA). The mouse hepatocyte cell line AML-12 was obtained from the American Type Culture Collection (ATCC, Manassas, VA, USA). C-Reactive protein (CRP) was obtained from Beyotime Biotechnology (Shanghai, China). Healthy rabbit blood was purchased from Saibekang.

2.2 Preparation of GalNAc(tri)–PEG2000–DSPE

The synthesis of DSPE–PEG2000–GalNAc(tri) was carried out *via* a KOH-mediated deacetylation reaction in anhydrous methanol. Specifically, peracetylated GalNAc(tri)–OAc–PEG2000–DSPE (20 mg, 1.0 equiv.) was dissolved in dry methanol, followed by dropwise addition of a methanolic solution of potassium hydroxide (KOH, 10 equiv.). The reaction mixture was stirred at room temperature for 24 h to ensure complete removal of the acetyl

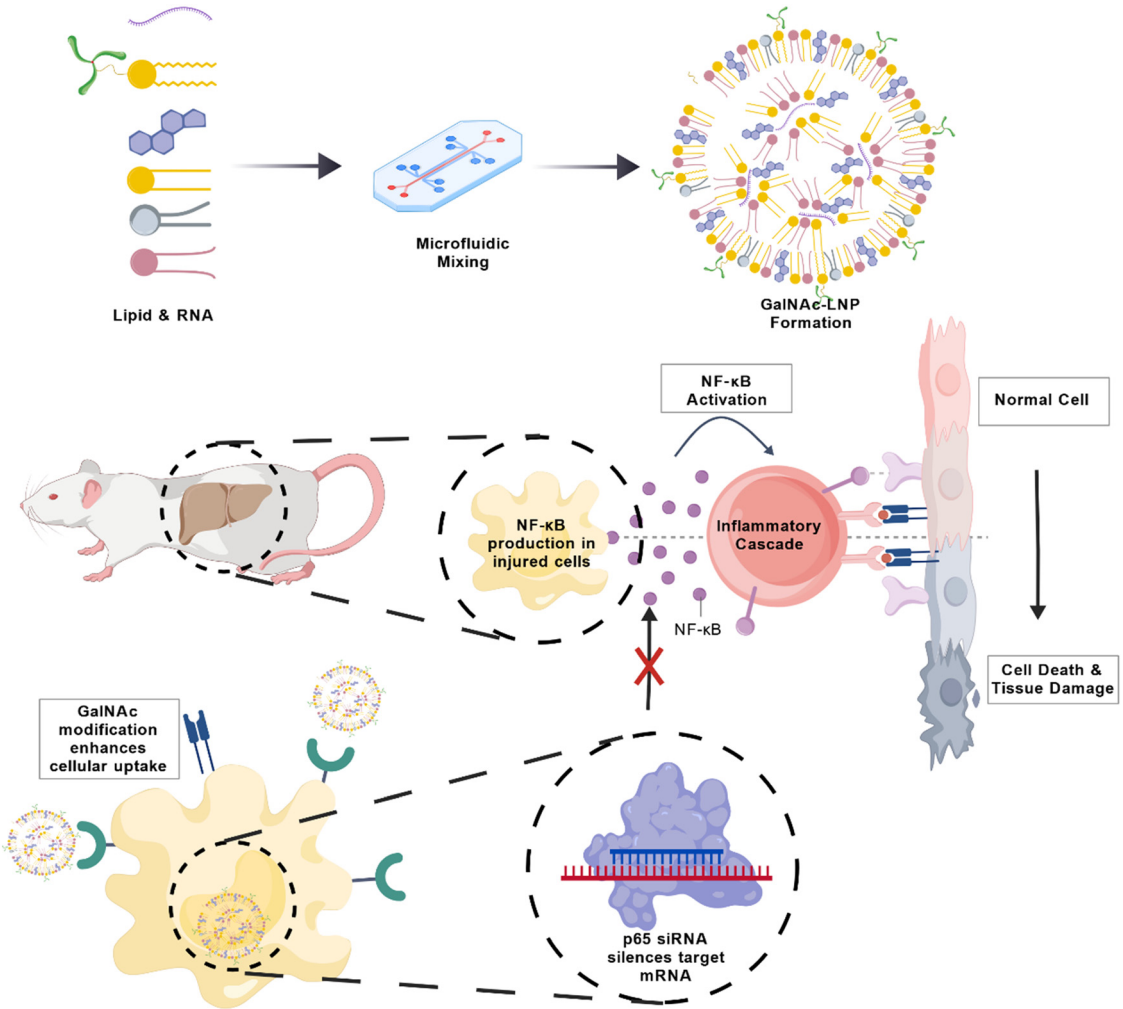

Scheme 1 The overall strategy for synthesizing GalNAc-functionalized lipid nanoparticles and their mechanism for targeted siRNA delivery to hepatocytes. The scheme outlines two main parts: (1) the chemical synthesis of the targeting ligand GalNAc(tri)–PEG2000–DSPE and its incorporation into LNPs *via* microfluidic mixing, and (2) the subsequent receptor-mediated uptake of GalNAc–LNPs by hepatocytes *via* ASGPR binding, followed by endosomal escape and siRNA-mediated knockdown of the target gene (p65/NF-κB) to alleviate inflammation.

protecting groups. After completion, the product was precipitated by dripping the mixture into ice-cold diethyl ether. The resulting solid was collected by centrifugation, washed thoroughly with cold ether, and then redissolved in pure water. Further purification was performed by dialysis against deionized water using a membrane with a molecular weight cut-off (MWCO) of 3.5 kDa for 24–48 h. Finally, lyophilization yielded GalNAc(tri)–PEG2000–DSPE as a white, solid product, whose structure was verified by ^{1}H NMR spectroscopy. ^{1}H NMR (400 MHz, DMSO-d_6, TMS): δ 4.49 (m, 1H, anomeric H-1 of GalNAc), 3.71–3.41 (br, –OCH_2CH_2– of PEG), 2.02 (s, residual –$COCH_3$, integration $<$0.2H relative to anomeric H), 1.23 (br, –CH_2– of DSPE alkyl chain), 0.85 (t, 3H, terminal –CH_3 of DSPE). The solvent residual signal appeared at δ 2.50 and the TMS reference at δ 0.00. The complete ^{1}H NMR spectrum is provided in Fig. 1B.

2.3 Preparation of GalNAc-functionalised LNPs

Lipid nanoparticles (LNPs) were synthesized *via* microfluidic mixing. The ionizable lipid DLin-MC3-DMA, DSPC, cholesterol, DMG–PEG2000, and GalNAc(tri)–PEG2000–DSPE were dissolved in ethanol at specified molar ratios (see the SI). The aqueous phase consisted of either mRNA encoding Luc mRNA or P65 siRNA dissolved in 50 mM citrate buffer (pH 4.0). A fixed mass ratio of ionizable lipid to RNA of 20 : 1 was maintained. Using a microfluidic module (FluidicLab), the ethanol phase and aqueous phase were mixed at a 3 : 1 volumetric flow rate ratio. The resulting mixture was purified by ultrafiltration at 3000 rpm for 30 min using Sartorius centrifugal filters (MWCO = 30 kDa, Biorigin). The purified LNPs were immediately diluted in phosphate-buffered saline (PBS, pH 7.4) for further characterization. The hydrodynamic diameter and polydispersity index (PDI) of the LNPs were measured at 25 °C using a Zetasizer Nano ZS (Malvern Instruments). Encapsulation efficiency was determined according to the manufacturer's protocol using the Quant-iT™ RiboGreen® RNA assay kit (R11490, Thermo Fisher Scientific, USA). The ionizable lipid DLin-MC3-DMA, DSPC, cholesterol, DMG–PEG2000, and GalNAc(tri)–PEG2000–DSPE were dissolved in ethanol at specified molar ratios. A base formulation

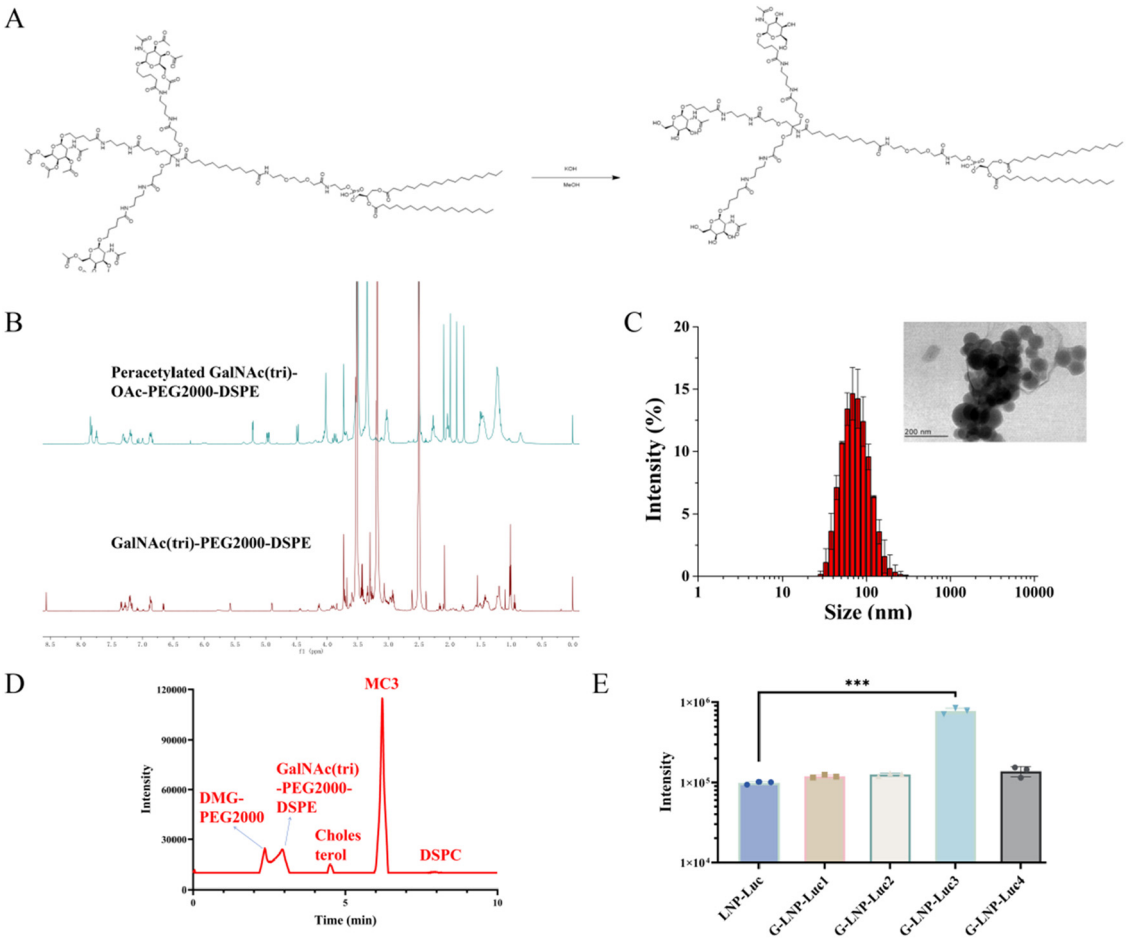

Fig. 1 (A) Synthetic route of GalNAc–PEG–DSPE; (B) ^{1}H NMR spectrum; (C) hydrodynamic diameter distribution and representative transmission electron microscopy (TEM) images of GalNAc–LNPs. Particle size data are presented as mean ± SD (n = 3).(D) LC-DAD chromatogram of the optimized GalNAc-LNP formulation (formulation 3) monitored at 210 nm. (E) Luciferase transfection efficiency. Data are presented as mean ± SD (n = 3); ***$p < 0.001$.

(formulation 1) consisted of MC3/DSPC/cholesterol/DMG–PEG2000 at a molar ratio of 50 : 10 : 38.5 : 1.5. To optimize the surface density of the targeting ligand, four additional formulations (formulations 2–5, designated as G-LNP1 to G-LNP4, respectively) were prepared by incorporating increasing amounts of DSPE–PEG2000–GalNAc(tri) (0.1%, 0.5%, 1%, and 2% of total lipid) while maintaining the other components at the same ratios as the base formulation.

To further investigate the impact of individual lipid component variations on LNP properties, five additional formulations (formulations 6–10) were prepared with the GalNAc–PEG2000–DSPE content fixed at 1 mol%, while systematically adjusting the ratios of MC3, DSPC, cholesterol, and DMG–PEG2000. The detailed molar ratios for all formulations are as follows: formulation 6 (G-LNP5): MC3 49%, DSPC 10%, cholesterol 38.5%, DMG–PEG2000 1.5%, GalNAc–PEG2000–DSPE 1%; formulation 7 (G-LNP6): MC3 50%, DSPC 10%, cholesterol 38.5%, DMG–PEG2000 0.5%, GalNAc–PEG2000–DSPE 1%; formulation 8 (G-LNP7): MC3 50%, DSPC 10%, cholesterol 37.5%, DMG–PEG2000 1.5%, GalNAc–PEG2000–DSPE 1%; formulation 9 (G-LNP8): MC3 50%, DSPC 9%, cholesterol 38.5%, DMG–PEG2000 1.5%, GalNAc–PEG2000–DSPE 1%; formulation 10 (G-LNP9): MC3 49.5%, DSPC 9.5%, cholesterol 38.5%, DMG–PEG2000 1.5%, GalNAc–PEG2000–DSPE 1%.

The aqueous phase consisted of either mRNA encoding Luc mRNA or P65 siRNA dissolved in 50 mM citrate buffer (pH 4.0). A fixed mass ratio of ionizable lipid to RNA of 20 : 1 was maintained. Using a microfluidic module (FluidicLab), the ethanol phase and aqueous phase were mixed at a 3 : 1 volumetric flow rate ratio. The resulting mixture was purified by ultrafiltration at 3000 rpm for 30 min using Sartorius centrifugal filters (MWCO = 30 kDa, Biorigin). The hydrodynamic diameter and polydispersity index (PDI) of the LNPs were measured at 25 °C using a Zetasizer Nano ZS (Malvern Instruments). Encapsulation efficiency was determined according to the manufacturer's protocol using the Quant-iT™ RiboGreen® RNA assay kit (R11490, Thermo Fisher Scientific, USA).

2.4 Characterisation approach for LNP nanocarriers

Transmission electron microscopy (TEM, Tecnai 12; Philips Company, Holland) was used to characterise the morphology of the GalNAc-LNP nanocarriers. The procedure was as follows: 10 μL of a nanoparticle suspension (1 mg mL^{-1}) was negatively stained with 2% phosphotungstic acid solution, subsequently

placed on a copper grid, and observed after drying at room temperature. Particle size distribution and zeta potential were measured using a Nano-ZS 90 dynamic light scattering instrument (Marvin Company). The measurements were performed in triplicate on an aqueous dispersion system at a concentration of 0.01 mg mL^{-1} under constant temperature conditions (25 °C). To evaluate the *in vitro* stability of the nanoparticles, the same instrument was used to monitor the GalNAc–LNP samples in PBS over a continuous 15 day period, assessing key parameters such as hydrodynamic diameter and PDI.

The synthesized GalNAc–PEG2000–DSPE and final LNP formulations were characterized by LC-DAD to confirm the identity and purity of the lipid components. Prior to analysis, the samples were lyophilized and the resulting powders were dissolved in acetonitrile, followed by thorough sonication to ensure complete disruption of the lipid nanoparticles. The analysis was performed on a Waters ACQUITY UPLC system coupled with a photodiode array (PDA) detector and a mass spectrometer. Chromatographic separation was achieved using a Welch C18 column (5 μm, 4.6 × 150 mm). The column temperature was maintained at 40 °C. The mobile phase consisted of solvent A (water with 0.1% formic acid) and solvent B (acetonitrile or methanol with 0.1% formic acid) at a flow rate of 0.5 mL min^{-1}. The following gradient program was applied: 0–2 min: 5% B; 2–5 min: 5–95% B; 5–8 min: 95% B; 8–10 min: 95–5% B. The PDA detector was set to monitor wavelengths between 210 and 400 nm, with the specific detection wavelength for lipid analysis at 210 nm. Data acquisition and processing were carried out using Waters Empower software.

2.5 Hemolysis assay

Healthy rabbit blood was defibrinated by shaking with glass beads, then washed with 0.9% sodium chloride solution by centrifugation (1000–1500 rpm, 15 min) until the supernatant was clear. The washed red blood cells were resuspended in 0.9% sodium chloride solution to obtain a 4% erythrocyte suspension.

The test sample was dissolved to 51.2 mg mL^{-1} as a stock solution. A two-fold serial dilution was performed in a 96-well plate to obtain sample concentrations ranging from 512 μg mL^{-1} to 0.5 μg mL^{-1}. The positive control, Triton-X-100, was similarly diluted to concentrations ranging from 2% to 0.002%. Each sample dilution, positive control, and negative control (0.9% sodium chloride solution) were mixed with an equal volume of the 4% erythrocyte suspension and incubated at 37 °C for 1 h. After centrifugation, the absorbance of the supernatant was measured at 540 nm using a microplate reader. The negative control was used for background correction, and the high-concentration positive control (2% Triton-X-100) served as the 100% hemolysis reference for calculating hemolysis percentages. For hematological analysis, blood samples were collected into EDTA-coated tubes, and complete blood counts, including white blood cell differentials, and red blood cell counts were measured using an automated hematology analyzer. Serum levels of C-reactive protein (CRP) were measured using enzyme-linked immunosorbent assay (ELISA) kits according to the manufacturer's instructions. Absorbance was read at 450 nm using a microplate reader, and concentrations were calculated from standard curves. All experimental procedures were performed in accordance with the Guidelines for the Care and Use of Laboratory Animals and approved by the Animal Care and Welfare Committee of Guangxi Medical University.

2.6 Bioinformatics analysis

To validate the expression stability of the asialoglycoprotein receptor (ASGPR) subunits in liver tissues under pathological conditions, bioinformatics analysis was performed using publicly available transcriptomic data. The gene expression dataset GSE179164 was downloaded from the Gene Expression Omnibus (GEO) database (https://www.ncbi.nlm.nih.gov/geo/). This dataset contains mRNA expression profiles of liver tissues from normal mice and mice with chemically-induced acute liver injury (ALI). The expression levels of the two major functional subunits of ASGPR, namely Asgr1 and Asgr2, were extracted and compared between the control group and the ALI model group.

2.7 Cellular experiments

2.7.1 Cell culture. The AML-12 cell revival and culture protocol involved rapidly thawing frozen cells in a 37 °C water bath, centrifuging to remove the cryoprotectant, and seeding into flasks containing DMEM/F12. The cells were incubated at 37 °C in a 5% CO_2 incubator, and cell attachment was observed 24 h post-revival. The medium was periodically refreshed, and the cells were passaged upon reaching 80–90% confluence, ensuring healthy cell growth for subsequent experiments.

2.7.2 CCK-8 experiment. To investigate the biological effects of the drug, the study focused on cellular viability, proliferation, and migration. AML-12 cells were cultured in DMEM containing 10% heat-inactivated FBS and 1% penicillin–streptomycin at 37 °C in a humidified 5% CO_2 incubator. Thereafter, DMEM supplemented with varying concentrations of the LNP (10 μg mL^{-1}, 100 μg mL^{-1}, 1000 μg mL^{-1}) was added to 96-well plates (10 000 cells per well). After 24 h of incubation with the medium, cell viability was assessed using the CCK-8 assay to evaluate the impact on cellular activity. All tests were conducted with six replicate wells, and the experiment was repeated three times independently.

2.7.3 *In vitro* transfection efficiency analysis by luciferase reporter assay. To evaluate the functional delivery of LNPs, AML-12 cells were seeded in 96-well plates at a density of 1×10^4 cells per well and incubated overnight. Cells were then treated with LNPs encapsulating Luc mRNA at final RNA doses of 12.5, 25, 50, and 100 ng per well. After 4 h of incubation, the medium was replaced with fresh complete medium. The cells were then cultured for an additional 24 h to allow for mRNA translation and luciferase expression. Subsequently, the cells were lysed using 1× Passive Lysis Buffer. A 20 μL aliquot of each lysate was transferred to a white, opaque 96-well assay plate. Luciferase activity was measured immediately after the automatic injection of 100 μL luciferase substrate using a multi-mode microplate reader. The chemiluminescence signal for each well was recorded.

To investigate the role of the ASGPR in mediating cellular uptake, cells were pre-treated for 1 hour with one of the two competitive inhibitors–asialofetuin (inhibitor1, 100 μg mL^{-1}) or free *N*-acetyl-D-galactosamine (inhibitor2, 20 mM)-prior to incubation with the LNPs. Subsequently, the cells were incubated with various formulations encapsulating Luc mRNA. These formulations included the commercial transfection reagent Lipofectamine 3000™ as a positive control, the experimentally designed GalNAc–LNPs, and the unmodified LNPs as a non-targeted control.

2.7.4 Quantitative analysis of oxidative stress and inflammatory cytokines in AML-12 cells. To establish an *in vitro* model of CCL_4-induced hepatocyte injury, AML-12 cells were cultured for 12 hours, after which the medium was replaced with fresh medium containing CCl_4 (10 mM). Following a 12 hour co-incubation, cell viability was assessed using the CCK-8 assay in 96-well plates. For biochemical analyses, the culture supernatant from 24-well plates was collected to measure aspartate aminotransferase (AST) activity. Cells were lysed to determine oxidative stress markers–malondialdehyde (MDA) content and superoxide dismutase (SOD) activity–using assay kits from Beyotime (China). The levels of pro-inflammatory cytokines (IL-6, TNF-α, and IL-1β) in the supernatant were quantified using ELISA kits from Elabscience (Shanghai, China). All procedures were performed strictly according to the manufacturers' protocols.

2.7.5 qRT-PCR analysis of NF-κB expression. The mRNA expression level of NF-κB in treated AML-12 cells was quantified by quantitative real-time polymerase chain reaction (qRT-PCR). Briefly, total RNA was extracted from the cell samples using TRIzol reagent (Invitrogen, San Diego, CA), and its concentration and purity were assessed with a NanoDrop spectrophotometer. Subsequently, first-strand cDNA was synthesized by reverse transcription using the TIANscript RT Kit (TianGen, China) according to the manufacturer's instructions. qRT-PCR was then performed on a Bio-Rad system using the resulting cDNA with gene-specific primers. The primers for the target gene NF-κB (forward: 5′-CCACGAGGCAGCACATAGAT-3′; reverse: 5′-GGTCCTTCCTGCCCATAACC-3′) and the internal control gene GAPDH (forward: 5′-AGGTCGGTGTGAACGGATTTG-3′; reverse: 5′-TGTAGACCATGTAGTTGAGGTCA-3′) were designed based on their respective mRNA sequences and synthesized by Nanning Jienisi Biotechnology Co., Ltd (Nanning, China). The mRNA expression levels were calculated using the $2^{-\Delta\Delta Ct}$ method.

2.8 *In vivo* biodistribution dynamics of nanoparticles

To evaluate the *in vivo* biodistribution and temporal dynamics of the nanoparticles, Balb/c mice were administered GalNAc–LNPs or unmodified LNPs encapsulating firefly luciferase (Fluc) mRNA *via* tail vein injection at a dose of 150 μg mRNA per kg body weight. At predetermined time points post-injection (1 and 8 h), mice were anesthetized and intraperitoneally injected with D-luciferin, potassium salt (150 mg kg^{-1}). Bioluminescence imaging was performed using an IVIS Spectrum *in vivo* imaging system (PerkinElmer, Waltham, MA, USA) 10 minutes after substrate administration. At the 1 h and 8 h time points, mice were euthanized following imaging, and major organs (liver, spleen, heart, lungs, and kidneys) were harvested for *ex vivo* imaging to quantify nanoparticle accumulation. The acquired bioluminescence signals were analyzed using Living Image software (PerkinElmer, Waltham, MA, USA).

2.9 Animals and acute liver injury model establishment

Six-week-old female BALB/c mice were obtained from Guangxi Medical University Laboratory Animal Center. The mice were housed in an environmentally controlled room (temperature: 22–24 °C, humidity: 60%) under a 12 h light/dark cycle. Twenty male BALB/c mice (8 weeks old) were randomly divided into four groups ($n = 5$ per group): a control group receiving olive oil vehicle (CO); a Model group induced by daily intraperitoneal (i.p.) injection of 20% CCl_4 in olive oil (LD, 0.6 μL g^{-1} body weight) for 7 days; a siRNA treatment group that, after CCl_4 modeling, received daily i.v. administration of LNP p65 siRNA (LNP–siP65, 0.4 mg kg^{-1}) for 7 days starting on day 2 post-modeling; and a GalNAc–LNP/siRNA treatment group that, following the same modeling protocol, received daily i.v. injections of GalNAc–LNP-encapsulated p65 siRNA (G-LNP–siP65, P65 siRNA = 0.4 mg kg^{-1}) for 7 days also beginning on day 2. Seventy-two hours after the final treatment, peripheral blood was collected from the orbital sinus under anesthesia, after which the mice were euthanized by CO_2 inhalation, and liver tissues were harvested for subsequent analysis. All experimental procedures were performed in accordance with the Guidelines for the Care and Use of Laboratory Animals and approved by the Animal Care and Welfare Committee of Guangxi Medical University.

2.10 Biochemical analysis

The extent of acute liver injury was comprehensively assessed by measuring serum levels of liver enzymes (ALT and AST), oxidative stress markers (MDA and SOD), and pro-inflammatory cytokines (IL-6, TNF-α, and IL-1β), along with histopathological evaluation of liver tissues (H&E staining). All analyses were performed according to the manufacturers' protocols, $n = 5$.

2.11 Statistical analysis

Homogeneity of variances was verified prior to conducting two-way ANOVA with *post hoc* pairwise comparisons. Data are expressed as mean ± SD. Statistical significance was denoted as follows: $^{*}p < 0.05$, $^{**}p < 0.01$, and $^{***}p < 0.001$.

2.12 Ethics statement

All animal experiments were approved by the Animal Care and Welfare Committee of Guangxi Medical University (Approval no. 202407025, 202503019 and 202603001).

3 Results

3.1 Preparation and characterisation of GalNAc–LNPs

As shown in Fig. 1A, the synthesis of DSPE–PEG2000–GalNAc(tri) involves deprotection and purification steps. Under alkaline conditions (KOH), the acetyl group (OAc) on the sugar ring of

the precursor DSPE–PEG2000–GalNAc is effectively removed. The reaction mixture is then filtered and dialyzed to obtain a high-purity product. Nuclear magnetic resonance (^{1}H NMR) analysis confirmed that compared to the starting raw material, the characteristic proton chemical shift in the sugar ring region moved toward higher fields after deprotection, and the proton signal corresponding to the acetyl group was 1.7% of its original intensity (Fig. 1B), confirming the removal of the OAc protecting group.

To optimize the formulation, lipid nanoparticles (LNPs) were assembled using microfluidics with varying ratios of DSPE–PEG2000–GalNAc(tri) (0.1%, 0.5%, 1%, and 2%) while maintaining a fixed DMG–PEG2000 content (Table 1). As shown in Fig. 1C, formulation exhibited monodisperse particle sizes with PDI values below 0.2. However, at the 2% ligand ratio, the particle size increased to 116.03 ± 0.82 nm, which was markedly larger than the other groups (78–88 nm). LC-DAD analysis was performed to confirm the identity and purity of lipid components in the optimized GalNAc–LNP formulation (formulation 3). As shown in Fig. 1D, all four lipid components—including GalNAc–PEG–DSPE, DSPC, cholesterol, and the ionizable lipid—were clearly resolved and detected at 210 nm. The well-separated peaks with appropriate retention times and good peak symmetry indicate successful chromatographic separation and high purity of the lipid components, confirming the integrity of the formulation. In parallel, luciferase transfection efficiency (Fig. 1E) demonstrated a concentration-dependent increase from 0.1% to 1%, with the highest efficiency observed at 1%. Further increasing the ligand ratio to 2% did not yield additional improvement. Based on these results, the 1% DSPE–PEG2000–GalNAc(tri) formulation was selected for subsequent studies, as it provided optimal transfection efficiency while maintaining favorable particle size characteristics.

3.2 Role of GalNAc-modified LNPs in cellular uptake and hepatic-targeted drug distribution

To further optimize the lipid formulation, a series of GalNAc-modified LNPs with varying lipid ratios were prepared and evaluated. As summarized in Table 2, all formulations exhibited favorable physicochemical properties, with particle sizes ranging from 62.5 nm to 180.7 nm and encapsulation efficiencies exceeding 90%.

While the safety of DSPE–PEG2000–GalNAc(tri) has been extensively validated, its biosafety within multi-component LNP systems requires systematic evaluation. To this end, we first performed cytotoxicity tests. Co-Incubation of LNPs at varying concentrations with AML-12 cells showed no significant impact on cell viability at low concentrations (Fig. 2B) and a trend toward cell proliferation was even at specific concentrations, which may be attributed to the inherent immunomodulatory properties of the LNPs. However, higher concentrations induced apoptosis (Fig. 2B). Importantly, these cytotoxic concentrations were substantially higher than the therapeutic doses used in subsequent delivery experiments, indicating they remained within a safe range. These results support our further functional validation.

Next, we investigated the effect of GalNAc modification on LNP transfection efficiency using luciferase (Luc) mRNA. LNPs encapsulating Luc mRNA without (LNP–Luc) or with GalNAc modification (G-LNP–Luc) were prepared. Given the nucleic acid's susceptibility to degradation and poor membrane permeability, we co-incubated these formulations with AML-12 cells and measured luciferase expression levels. The results showed that G-LNP–Luc significantly enhanced transfection efficiency in hepatocytes across all tested concentrations compared to unmodified LNP–Luc (Fig. 2C). The enhancement was most pronounced at the highest concentration, where the optimal G-LNP–Luc formulation (G-LNP–Luc8) exhibited luminescence intensity over 2.8-fold higher than the unmodified LNP–Luc group. Bioinformatic analysis of the GEO dataset GSE179164 revealed no statistically significant difference in the mRNA expression levels of the key targeting receptors Asgr1 and Asgr2 between normal and chemically-induced acute liver injury mouse models. This indicates stable basal expression of the ASGPR-mediated endocytic pathway under the injury conditions used, providing a feasible basis for the subsequent GalNAc–LNP targeting strategy (Fig. 2D). *In vitro* transfection experiments demonstrated that G-LNP–Luc delivered Luc mRNA with significantly higher efficiency than unmodified LNP–Luc, in both normal AML-12 hepatocytes and liver injury (LD) cell models. Notably, G-LNPs showed consistently superior performance across both physiological states. This suggests that the enhancement is primarily due to the inherent ASGPR-targeting capability of G-LNP–Luc, rather than being dependent on injury-induced microenvironmental changes, proving their stable and superior delivery potential under both normal and disease conditions (Fig. 2E).

To determine whether this effect was mediated by ASGPR, we conducted blocking experiments using ASGPR inhibitors. Pre-treatment with inhibitors significantly reduced the chemiluminescence intensity of the G-LNP–Luc group, while the

Table 1 Physicochemical characterization of GalNAc–LNP formulations

Name	Particle size (nm)	PDI	Zeta potential (mV)	Encapsulation efficiency (%)
LNP–Luc	78.15 ± 0.39	0.130 ± 0.008	0.12 ± 0.35	92.18 ± 1.40
G-LNP–Luc1	78.97 ± 0.88	0.137 ± 0.012	0.67 ± 0.48	91.27 ± 0.94
G-LNP–Luc2	87.33 ± 0.33	0.146 ± 0.012	1.01 ± 0.70	90.54 ± 1.11
G-LNP–Luc3	87.23 ± 1.03	0.146 ± 0.010	0.03 ± 0.73	90.07 ± 0.92
G-LNP–Luc4	116.03 ± 0.82	0.132 ± 0.007	0.27 ± 1.03	89.20 ± 1.23

Table 2 Physicochemical characterization of GalNAc–LNP formulations

Formulation	Particle size (nm)	PDI	Zeta potential (mV)	Encapsulation efficiency (%)
LNP–Luc	74.2 ± 1.9	0.161 ± 0.012	0.38 ± 0.63	92.46 ± 0.92
G-LNP–Luc6	65.1 ± 1.9	0.091 ± 0.039	0.10 ± 0.82	92.66 ± 1.08
G-LNP–Luc7	180.7 ± 4.5	0.192 ± 0.031	−0.12 ± 0.59	91.54 ± 1.17
G-LNP–Luc8	68.9 ± 0.7	0.122 ± 0.035	−0.25 ± 1.00	90.94 ± 2.03
G-LNP–Luc9	62.5 ± 1.0	0.089 ± 0.038	−0.35 ± 0.48	90.27 ± 3.50
G-LNP–Luc10	72.3 ± 1.7	0.158 ± 0.040	−0.04 ± 1.44	93.23 ± 2.22

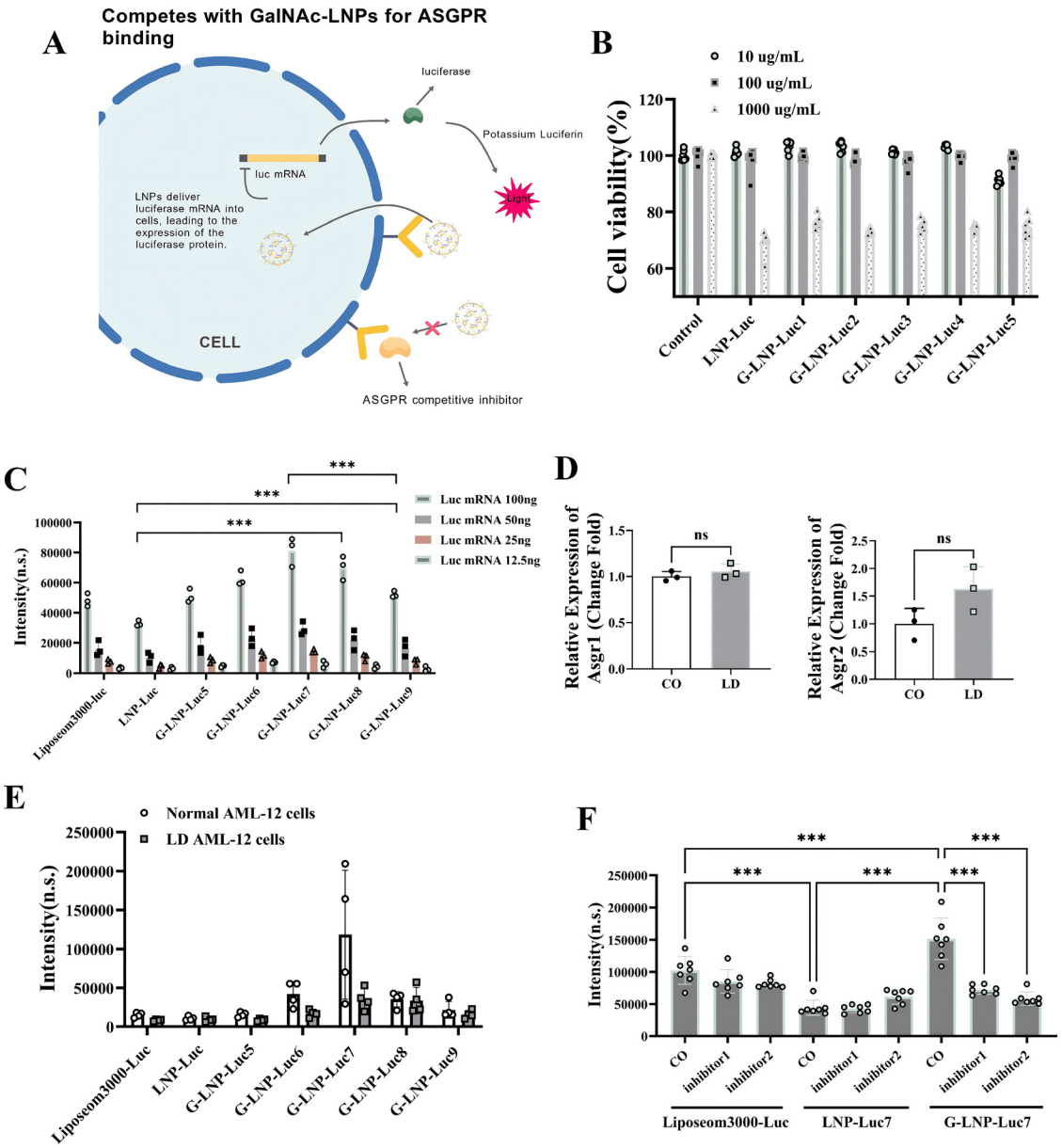

Fig. 2 (A) Schematic illustration of the experimental design. (B) Cytotoxicity assessment: cell viability after 24 hour incubation with various concentrations of different materials. (C) Transfection efficiency: luminescence intensity in cells transfected with LNPs encapsulating Luc–mRNA at different concentrations. (D) Bioinformatics analysis of hepatic Asgr1 and Asgr2 expression. (E) Target validation: changes in luminescence intensity following pre-treatment with an ASGPR competitive inhibitor. (F) Transfection efficiency of Luc mRNA-loaded LNPs and G-LNPs in normal and LD model cells. Data are presented as mean ± SD; ***$p < 0.001$, "ns" indicates no statistical difference.

unmodified LNP–Luc group showed no significant change (Fig. 2F). This confirms that the addition of DSPE–PEG2000–GalNAc(tri) enhances hepatocyte targeting and endocytosis of LNPs *via* the ASGPR pathway.

3.3 p65 siRNA-mediated attenuation of inflammation in injured hepatocytes

As summarized in Table 3, both LNP–siP65 and G-LNP–siP65 showed comparable and favorable physicochemical characteristics, including particle sizes of approximately 90–96 nm, low polydispersity indices (<0.15), near-neutral zeta potentials, and encapsulation efficiencies above 76%, confirming the successful preparation of stable siRNA-loaded lipid nanoparticles. In this section, a hepatocyte injury model was established by stimulating AML-12 cells with CCl_4 stimulus, and the effects of different LNP–siP65 complexes on cell viability, oxidative stress, and inflammatory cytokine secretion were evaluated. Overall results demonstrated that G-LNP–siP65 significantly improved the viability of injured hepatocytes, increasing cell activity by approximately 18% ($p < 0.01$) compared with the inflammatory model group (Fig. 3A). Compared with the untreated or empty LNP control groups, treatment

Table 3 Physicochemical characterization of GalNAc–LNP formulations

Formulation	Particle size (nm)	PDI	Zeta potential (mV)	Encapsulation efficiency (%)
LNP–siP65	95.86 ± 0.29	0.142 ± 0.008	0.37 ± 0.30	76.70 ± 0.84
G-LNP–siP65	90.75 ± 0.83	0.122 ± 0.020	−0.78 ± 0.51	81.63 ± 3.27

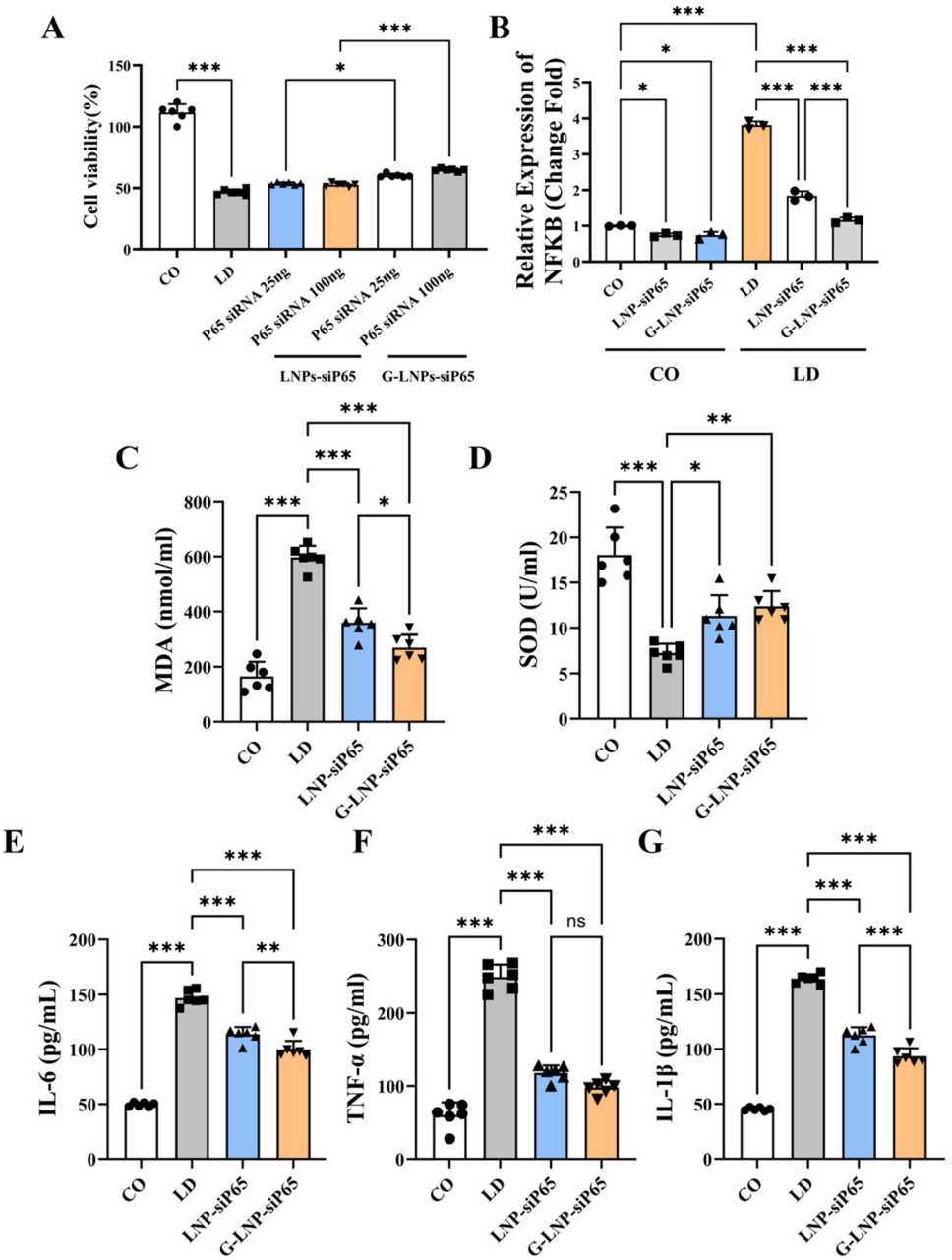

Fig. 3 (A) Cell viability under different treatment conditions. (B) qRT-PCR analysis of p65 mRNA expression in injured cells transfected with different formulations of LNPs encapsulating p65 siRNA at varying concentrations. (C) MDA content, (D) SOD activity, (E) IL-6, (F) TNF-α, and (G) IL-1β. Data are presented as mean ± SD; *$p < 0.05$, **$p < 0.01$, ***$p < 0.001$, "ns" indicates no statistical difference.

with LNPs encapsulating p65 siRNA significantly down-regulated the mRNA expression level of p65 in injured cells, and this effect was concentration-dependent. This demonstrates that the designed LNPs can effectively deliver siRNA and silence the target gene (Fig. 3B). Meanwhile, G-LNP–siP65 treatment markedly alleviated the redox imbalance in the acute liver injury (ALI) model. SOD activity in the G-LNP–siP65 group rose to 12.38 U mL^{-1}, significantly higher than that in the

LNP–siP65 group (11.31 U mL^{-1}, $p < 0.05$, Fig. 3D). Correspondingly, the MDA level decreased to 269.45 nmol mL^{-1}, also significantly lower than that in the LNP–siP65 group (359.02 nmol mL^{-1}, $p < 0.05$) (Fig. 3C). The restoration of SOD activity together with the reduction in the MDA level indicates that G-LNP–siP65 effectively mitigates ALI-induced oxidative stress. In the effectively treated groups, the release of the pro-inflammatory cytokine IL-6 was significantly reduced. This indicates that the LNP–siRNA system alleviates the inflammatory response in cells by inhibiting the NF-κB signaling pathway, for which p65 is a key subunit (Fig. 3E). Consistent with the results for IL-6, the level of another key pro-inflammatory factor, TNF-α, also showed a significant decreasing trend. This further confirms that inhibiting p65 can broadly mitigate the inflammatory cytokine storm triggered by injury (Fig. 3F). The synergistic improvement of oxidative stress and inflammatory markers suggests that G-LNP–siP65 may simultaneously regulate two major pathological processes–oxidative stress and inflammatory response–by efficiently silencing NF-κB p65 at this key regulatory node. This not only confirms the pivotal role of the NF-κB pathway in linking oxidative stress to inflammatory responses but also highlights the enhanced therapeutic potential of the G-LNP–siP65 delivery system, which achieves superior gene silencing and improved therapeutic outcomes through optimized liver targeting.

3.4 Role of GalNAc-modified LNPs in hepatic-targeted distribution *in vivo*

To systematically compare the liver-targeting efficiency of different delivery systems, this study prepared both GalNAc-modified and unmodified Luc–mRNA LNPs (G-LNP–Luc and LNP–Luc) and evaluated their *in vivo* distribution and targeting efficacy using a small animal *in vivo* imaging system. As shown in Fig. 4A, representative whole-body bioluminescence images revealed that G-LNP–Luc exhibited stronger and more sustained liver signal compared to LNP–Luc. Quantitative analysis of total body bioluminescence flux (Fig. 4B) confirmed that G-LNP–Luc achieved significantly higher peak signals and prolonged retention. *Ex vivo* imaging of major organs at 1 h and 8 h post-injection (Fig. 4C) demonstrated that G-LNP–Luc predominantly accumulated in the liver, with minimal signal detected in other organs. Quantification of organ-associated bioluminescence signals based on average radiance (Fig. 4D and E) further validated that G-LNP–Luc showed markedly higher hepatic accumulation than LNP–Luc at both time points. These results confirm that GalNAc modification significantly enhances the hepatic accumulation and retention of LNPs, providing an optimized strategy for liver-targeted nucleic acid delivery. This enhanced targeting is consistent with the known high-affinity binding of GalNAc to the asialoglycoprotein receptor (ASGPR), which is abundantly expressed on hepatocytes, thereby facilitating receptor-mediated uptake.

3.5 *In vitro* hemolysis and *in vivo* safety evaluation

The hemolytic activity of LNP–siP65 and G-LNP–siP65 was evaluated using a rabbit erythrocyte model. As shown in Fig. 5A and B, the positive control (Triton X-100) induced complete hemolysis, whereas both LNP–siP65 and G-LNP–siP65 exhibited negligible hemolysis rates below 3% at the working concentrations, comparable to the negative control, indicating no hemolytic activity at the intended therapeutic doses.

Systemic inflammation was assessed by measuring serum C-reactive protein (CRP). As shown in Fig. 5C, CRP levels were significantly elevated in the LD group compared to the CO group. Treatment with LNP–siP65 moderately reduced CRP, while G-LNP–siP65 led to a more pronounced reduction, with levels approaching those of the CO group, confirming the superior anti-inflammatory effect of GalNAc-modified LNPs.

Hematological analysis (Fig. 5D–I) revealed that the model group exhibited a marked increase in both neutrophil percentage (Neu%, Fig. 5D) and absolute neutrophil count (NEU#, Fig. 5E) compared to the CO group. Treatment with LNP–siP65 partially reduced these elevated neutrophil parameters, and G-LNP–siP65 further lowered them to levels close to the CO group, demonstrating that GalNAc modification mitigates the neutrophil response without inducing additional inflammation. White blood cell (WBC) counts (Fig. 5F) were significantly increased in the model group but returned to normal levels after both treatments, with G-LNP–siP65 showing a slightly better restoration. No statistically significant differences were observed among the four groups in red blood cell counts (RBC, Fig. 5G), hematocrit (HCT, Fig. 5H), or hemoglobin (HGB, Fig. 5I), indicating that the LNP treatments did not adversely affect erythrocyte parameters.

Collectively, these results demonstrate that GalNAc modification reduces the pro-inflammatory impact of LNP administration, as evidenced by lower neutrophil counts and decreased serum CRP levels, while both formulations exhibit no hemolytic activity and preserve normal erythrocyte indices.

3.6 *In vivo* therapeutic efficacy of GalNAc–LNPs delivering p65 siRNA in an acute liver injury model

To validate the experimental design and treatment regimen, the detailed schematic is presented in Fig. 6A. In terms of hepatic tissue changes, compared to the control group, the model group exhibited significant liver tissue damage, characterized by marked hepatomegaly, a reddish-brown discoloration, and a hardened texture (Fig. 6B). Based on bio-distribution characteristics and biochemical indicators, we systematically evaluated the therapeutic potential of G-LNP–siP65 in the ALI mouse model. The ALI model was successfully established by intraperitoneal injection of CCl_4. In the model group, serum levels of key liver injury markers (ALT and AST) were significantly elevated compared with the control group (Fig. 6C and D). This confirmed the successful induction of the ALI mouse model, which exhibited severe hepatic dysfunction.

To evaluate the therapeutic efficacy of the targeted delivery system, we administered LNP–siP65 and G-LNP–siP65 to ALI mice. Both treatments partially attenuated CCL_4-induced liver dysfunction, oxidative stress, and inflammatory responses. However, the data clearly showed that G-LNP–siP65 outperformed

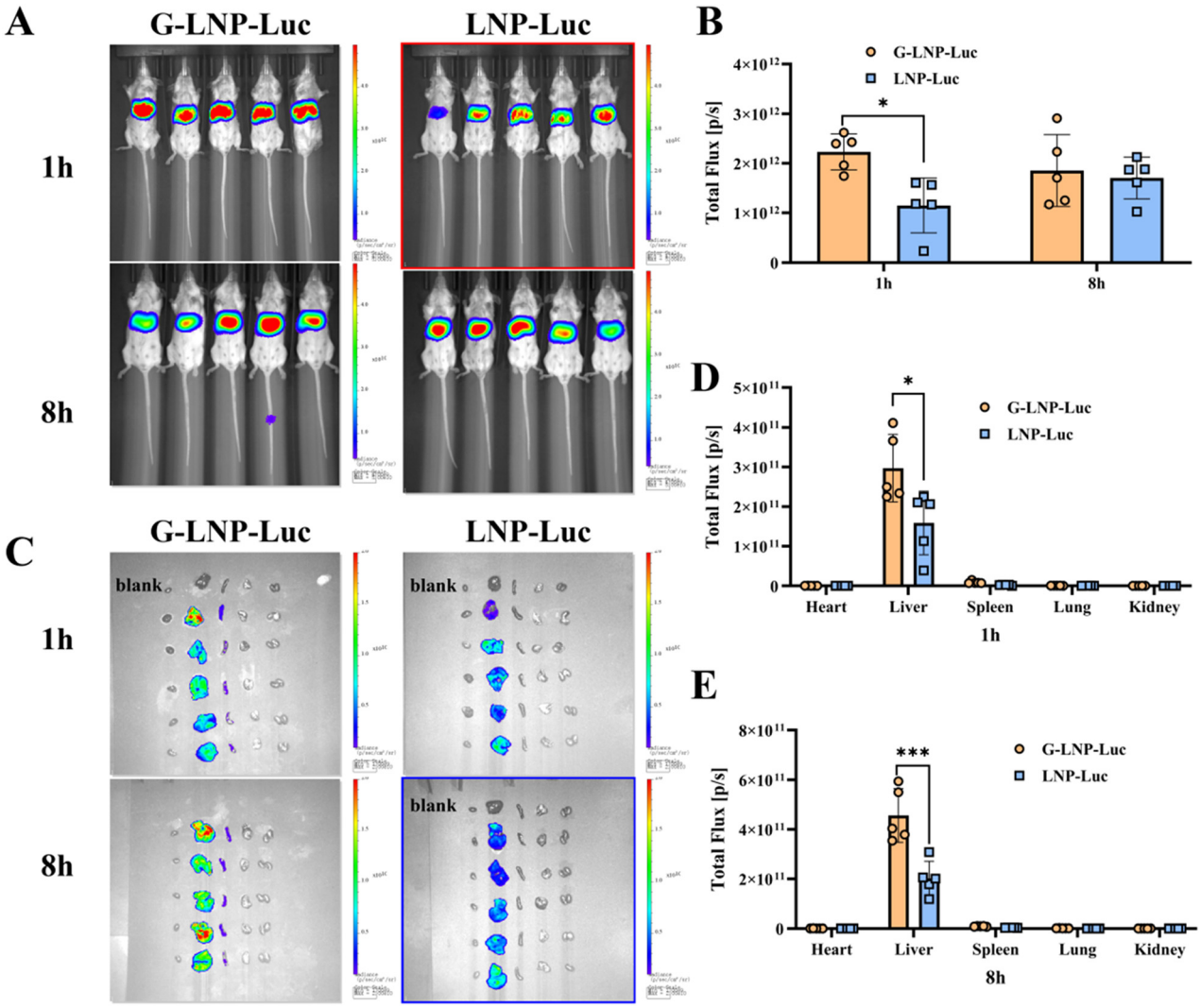

Fig. 4 (A) Representative whole-body bioluminescence images of mice at the indicated time points post-injection of LNPs encapsulating Luc mRNA. (B) Quantitative analysis of total body bioluminescence flux over time. (C) *Ex vivo* bioluminescence images of major organs (liver, spleen, heart, lungs, and kidneys) harvested at 1 and 8 h post-injection. (D) Quantification of organ-associated bioluminescence signals based on average radiance at 1 h post-injection. (E) Quantification of organ-associated bioluminescence signals based on average radiance at 8 h post-injection. Data are presented as mean ± SD; $*p < 0.05$, $***p < 0.001$, $n = 5$.

LNP–siP65 across all improvement parameters. This finding aligns with our cellular observations of the superior cellular uptake and gene silencing effects of G-LNP–siP65, providing preliminary evidence for the effectiveness of liver-targeted modification *in vivo*.

Among all treatment groups, G-LNP–siP65 demonstrated the most significant therapeutic effects. In terms of liver function improvement, G-LNP–siP65 more effectively reduced serum AST and ALT levels, with improvement rates ranging from approximately 31.7% to 46.5% compared to LNP–siP65 (Fig. 6C and D). Regarding oxidative stress regulation, SOD activity in the model group plummeted to 20% of that in the control group, while MDA levels surged to 284.9% of the control levels. After G-LNP–siP65 intervention, SOD activity recovered to 61.4% of the control level, and MDA content decreased to 139.3% of the control (Fig. 6E and F). These results were significantly better than those in the LNP–siP65 group, in which SOD activity recovered to 35.8% of the control level and MDA content was 191.5% of the control ($p < 0.01$). Thus, G-LNP–siP65 exhibited superior performance in restoring redox balance, indicating its greater efficacy in alleviating oxidative damage to hepatocytes.

Additionally, G-LNP–siP65 demonstrated strong capacity to suppress the inflammatory response. Compared to the ALI model group, treatment with G-LNP–siP65 significantly reduced the levels of key pro-inflammatory cytokines–TNF-α, IL-1β, and IL-6–by 37.5%, 41.4%, and 38.37%, respectively ($p < 0.05$). Its inhibitory effects were superior to those of the LNP–siP65 group, which achieved reductions of 31.1%, 29.4%, and 34.3%, respectively (Fig. 6G–I).

In summary, by efficiently delivering siP65 to the liver, G-LNP–siP65 significantly inhibited the activation of the NF-κB signaling pathway, thereby curbing the occurrence of a

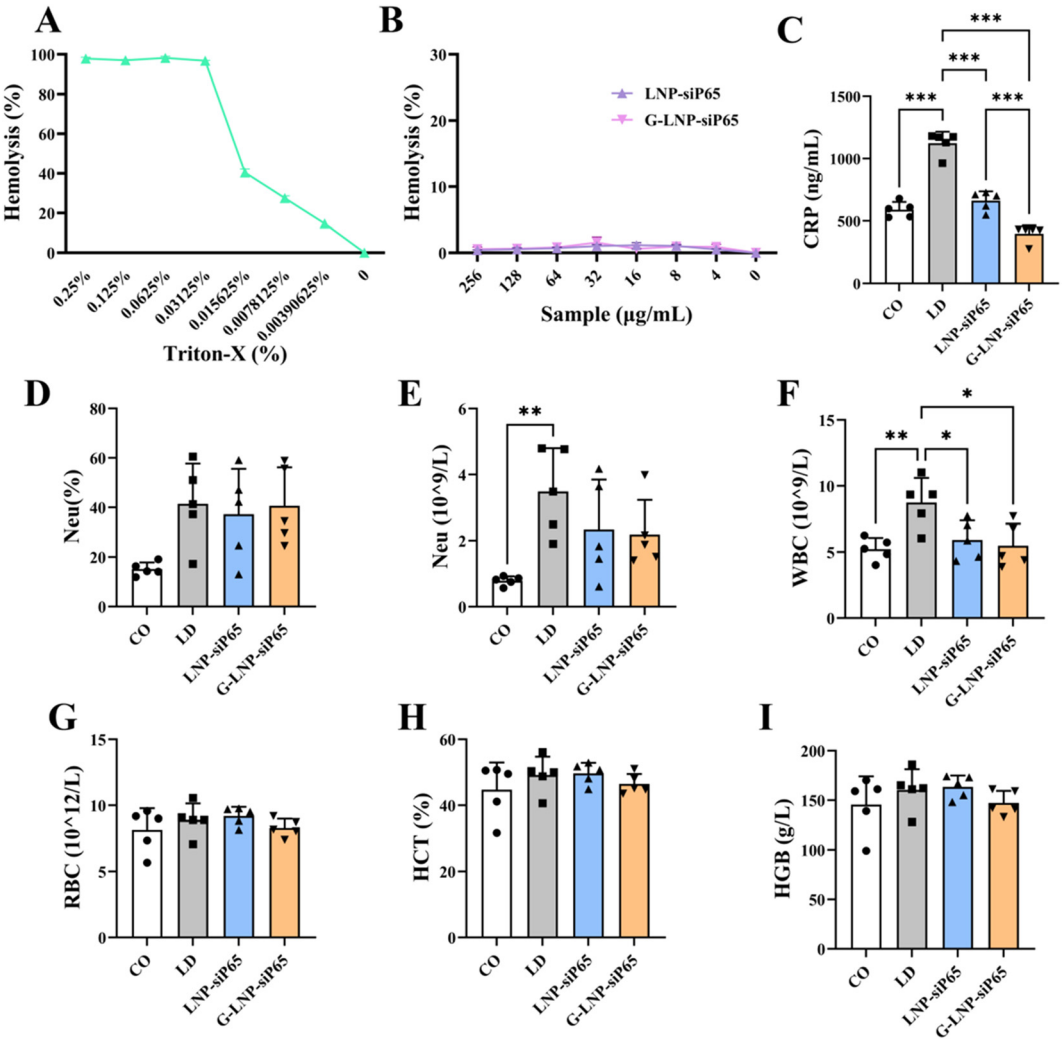

Fig. 5 (A) Hemolysis assay – positive control. Triton X-100 induced complete hemolysis. (B) Hemolysis assay – test formulations. Both LNP–siP65 and G-LNP–siP65 exhibited negligible hemolysis at the working concentrations, comparable to the negative control. (C) Serum C-reactive protein (CRP) levels. (D) Neutrophil percentage (Neu%). (E) Absolute neutrophil count (NEUT#). (F) White blood cell (WBC) count. (G) Red blood cell (RBC) count. (H) Hematocrit (HCT). (I) Hemoglobin (HGB). Data are presented as mean ± SD (n = 5 per group). Statistical significance was determined by one-way ANOVA followed by Tukey's *post hoc* test. *$p < 0.05$, **$p < 0.01$, and ***$p < 0.001$ compared to the model group (LD). CO: normal control; LD: CCl_4-induced acute liver injury model; LNP–siP65: non-targeted LNP encapsulating p65 siRNA; G-LNP–siP65: GalNAc-modified LNP encapsulating p65 siRNA.

"cytokine storm" at the transcriptional level. This mechanism is likely central to its efficacy in alleviating ALI.

The comprehensive therapeutic advantages exhibited by G-LNP–siP65 largely stem from its efficient liver-targeted delivery capability. In recent years, GalNAc-based siRNA delivery technology has marked a significant breakthrough in targeted therapy for liver diseases, becoming a key pillar of the "third wave" of modern nucleic acid therapeutics, following small molecules and antibody drugs.[37] The findings of this study align closely with this field-wide trend. Through GalNAc modification, we significantly enhanced the specific enrichment of LNPs in liver tissue. This enhancement is not merely a simple aggregation of the drug; more importantly, by improving hepatic retention and stability, it directly increases the drug's bioavailability, thereby achieving superior gene silencing and disease mitigation outcomes.

3.7 Histopathological and molecular analyses of liver tissues following GalNAc–LNP/p65 siRNA therapy in ALI mice

Representative images are shown in Fig. 7A. Successful establishment of the ALI model was confirmed by both biochemical and histopathological analyses. In model group mice, tissue levels of MDA and pro-inflammatory cytokines (TNF-α, IL-1β, and IL-6) were significantly elevated by 1.8–4.4-fold, while SOD activity decreased to 39.9% of control levels (Fig. 7D–H). H&E staining further revealed disorganized hepatic architecture, hepatocyte swelling with nuclear pyknosis or vacuolation, and extensive inflammatory cell infiltration (Fig. 7A). The corresponding liver injury score was significantly higher than that of the control group (Fig. 7B). All therapeutic interventions demonstrated ameliorative effects, among which treatment with GalNAc-LNP/p65 siRNA (G-LNP–siP65) was the most pronounced. At the molecular level, qRT-PCR analysis validated that G-LNP–siP65 more effectively

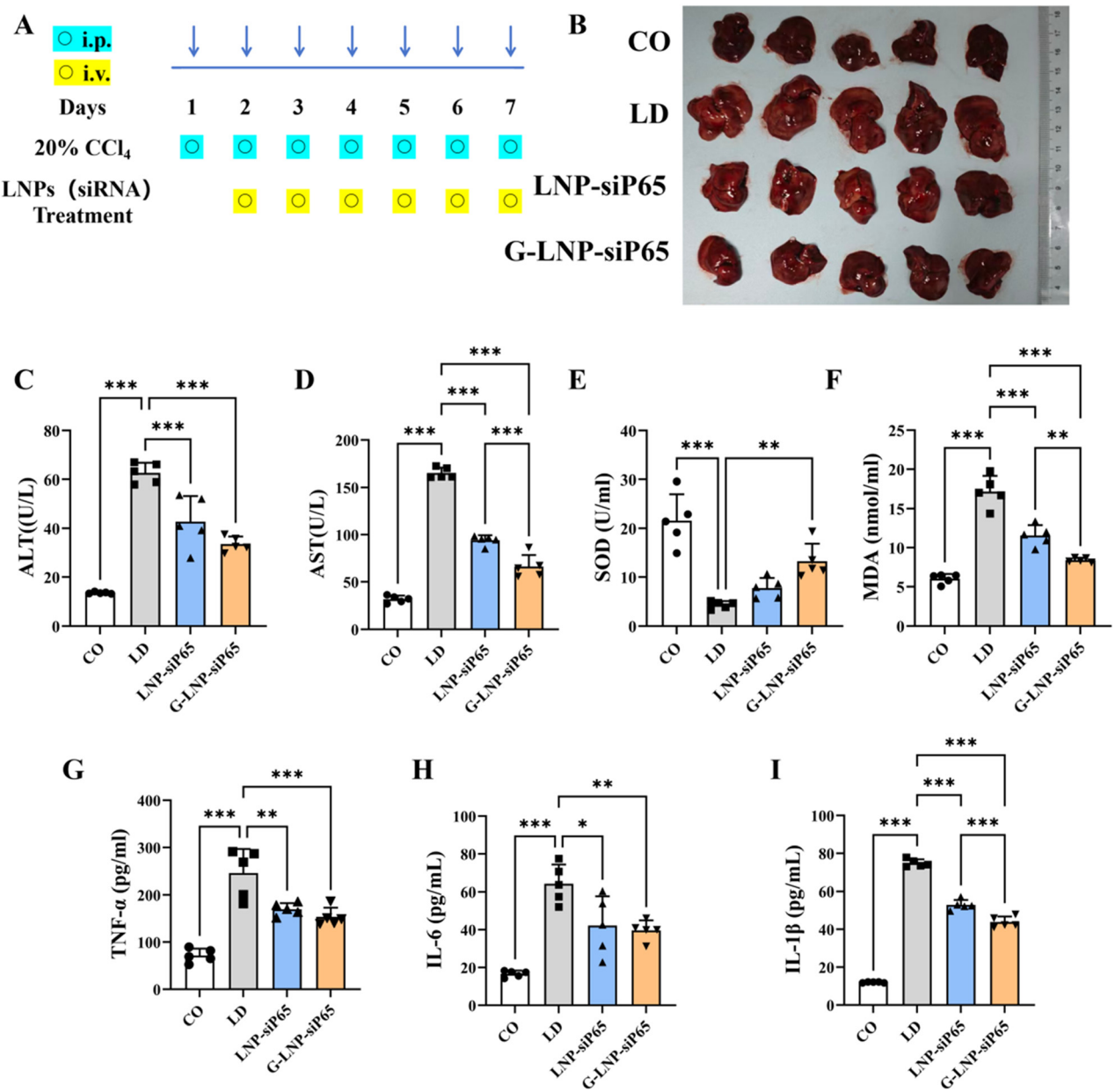

Fig. 6 (A) Schematic illustration of the experimental design and treatment timeline. (B) Representative photographs showing the gross appearance of mice from different groups; (C) ALT; (D) AST; (E) SOD activity, (F) MDA content, (G) TNF-α, (H) IL-6, and (I) IL-1β levels. Data are presented as mean ± SD; *$p < 0.05$, **$p < 0.01$, and ***$p < 0.001$.

suppressed the expression of NF-κB in liver tissue compared to the unmodified LNP/p65 siRNA (LNP–siP65) group ($p < 0.05$, Fig. 7C), providing an upstream mechanistic basis for the observed phenotypic improvements. Regarding the regulation of oxidative stress, G-LNP–siP65 treatment restored hepatic SOD activity to 64.7% of the normal level, an effect superior to that of the LNP–siP65 group (53.6%, $p < 0.05$). Concurrently, it reduced MDA content to 113.5% of the control, significantly lower than the 132.9% observed in the LNP–siP65 group (Fig. 7D and E).

In terms of anti-inflammatory efficacy, G-LNP–siP65 significantly reduced the levels of pro-inflammatory cytokines compared to the ALI model group, with reductions of 38.4% for TNF-α, 51.2% for IL-1β, and 57.9% for IL-6 ($p < 0.001$). This overall effect outperformed that of LNP–siP65, which achieved reductions of 26.5%, 17.2%, and 54.0%, respectively (Fig. 7F–H). The superior therapeutic efficacy of G-LNP–siP65 observed in this study in the aforementioned study is largely attributed to its highly efficient liver-targeted delivery capability. Previous research has confirmed that GalNAc-modified LNP systems can significantly enhance nanoparticle accumulation in the liver and cellular internalization efficiency by specifically recognizing the high-expressing ASGPR on hepatocytes.[38] The GalNAc modification strategy employed in this study is precisely based on this principle, aiming to optimize delivery precision and therapeutic

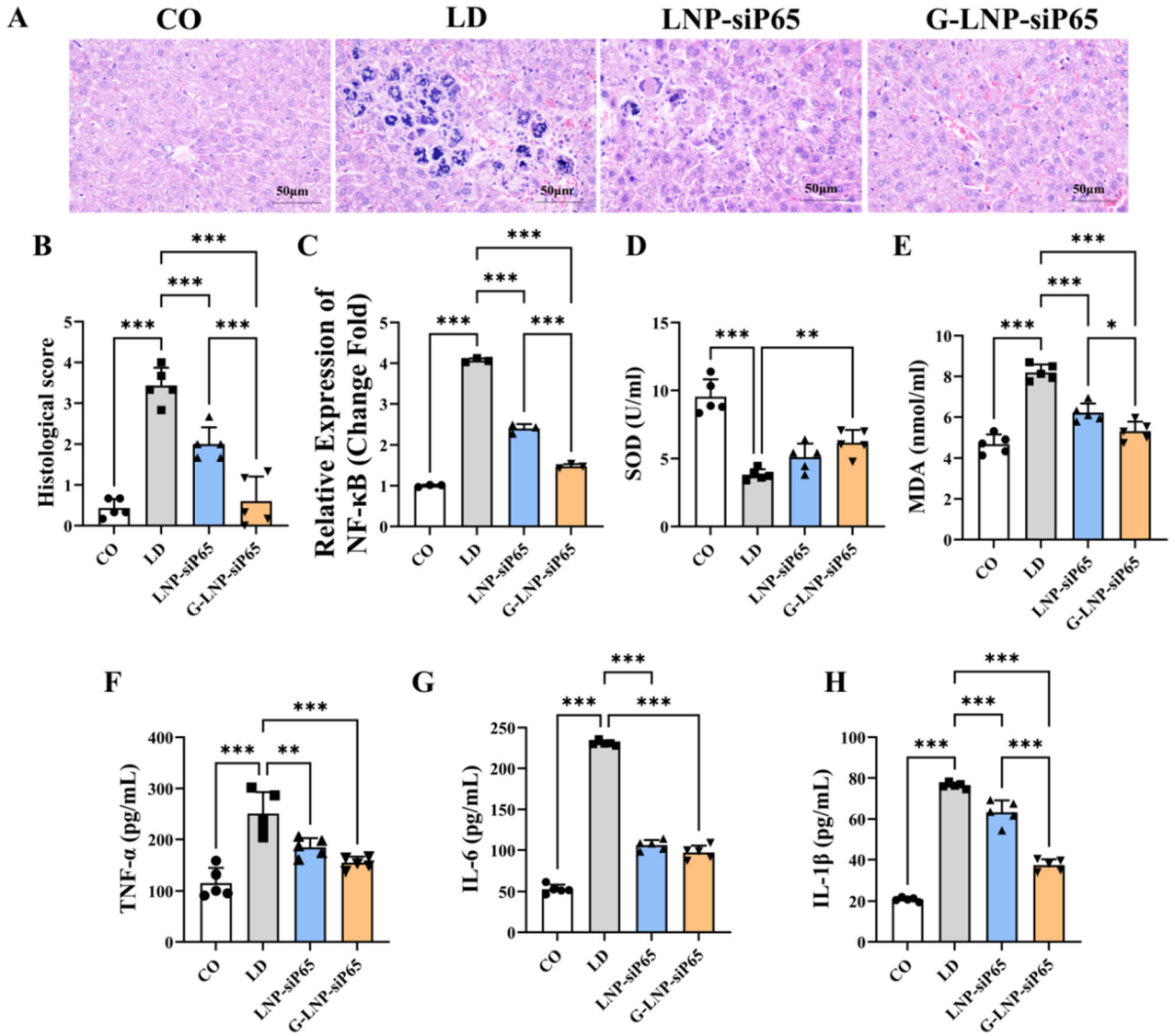

Fig. 7 (A)Representative H&E staining of liver sections (scale bar, 50 μm). (B) Histopathological injury score based on H&E staining. (C) Hepatic Nfkb1 mRNA expression level by qRT-PCR. (D) SOD activity, (E) MDA content, (F) TNF-α, (G) IL-6, and (H) IL-1β levels. Data are presented as mean ± SD; $*p < 0.05$, $**p < 0.01$, and $***p < 0.001$.

outcomes. In fact, similar liver-targeting strategies have been successfully translated into clinical applications. Multiple siRNA therapies based on covalently linked GalNAc delivery systems have entered clinical use, including GalNAc-conjugated agents for anticoagulation in patients at risk of thrombosis/thromboembolism. Examples include GalNAc-conjugated siRNA RBD4059, which targets and inhibits FXI protein synthesis in liver[39] and plozasiran.[40] These agents achieve efficient liver targeting and long-term gene silencing through subcutaneous injection, significantly advancing innovations in liver disease management.

4 Conclusion

This study systematically elucidated the multidimensional protective mechanisms of G-LNP–siP65 against ALI through an integrated, multi-level evaluation framework. The experimental results demonstrated that the delivery system not only effectively reversed hepatic injury at the histopathological level but also significantly suppressed inflammatory responses and restored redox balance. Furthermore, both *in vitro* hemolysis assay and *in vivo* hematological parameters showed no abnormalities, indicating good biosafety. Collectively, these findings offer critical evidence for advancing efficient gene-based intervention therapies *via* liver-targeted delivery systems, further highlighting the distinct advantages and broad translational potential of the GalNAc–LNP platform in targeted treatment of liver diseases. More broadly, this work exemplifies a rational design strategy to enhance the specificity and efficacy of nucleic acid therapeutics, opening avenues for developing more effective and clinically viable targeted therapies against hepatic diseases.

Author contributions

Zhijie Liang: investigation, methodology, formal analysis, writing – original draft. Shaorong Li: investigation, methodology, formal analysis, writing – original draft. Huali Huang: conceptualization, supervision, project administration, writing – review & editing. Shuying Luo: investigation, validation, writing – original draft. Hongmian Jiang: resources, funding acquisition. Lifeng Luo: resources, investigation. Jinzhuai Li: conceptualization, methodology, formal analysis, writing – review & editing. Kun Zhao: conceptualization, supervision, funding acquisition, writing – review & editing.

Conflicts of interest

The authors declare that there are no conflicts of interest.

Data availability

The data supporting this article have been included as part of the supplementary information (SI). Source data for all figures and tables are presented within the main text and are also provided in the SI. Supplementary information is available. See DOI: https://doi.org/10.1039/d6tb00003g.

Acknowledgements

This work was supported by the Middle/Young aged Teachers' Research Ability Improvement Project of Guangxi Higher Education (grant no. 2024KY0103); self-funded research project of Health Commission of Guangxi Zhuang Autonomous Region (grant no. Z-A20231144, Z-A20240991, Z-A20230481, and Z-A20240987); Self-funded research project of Administration of Traditional Chinese Medicine of Guangxi Zhuang Autonomous Region (grant no. GXZYA20240466, GXZYA20240462, GXZYA20240467); The key clinical specialist pathology unit program of Guangxi Zhuang Autonomous Region (grant no. 2023QZD01); the key Research and Development Project of Nanning Science and Technology Bureau (grant no. 20253036-2); and Open Project of Guangxi Key Laboratory of Basic Research on Enhanced Recovery After Surgery for Gastrointestinal Tumors (grant no. GXEKL202301).

References

1 Y. Chen, Y. Lei, H. Wang, L. Wang, J. Xu, S. Wang, M. Yu, Z. Peng, F. Xiao and D. Tian, *Int. J. Mol. Med.*, 2023, **52**, 78.
2 S. S. Pedersen, M. Prause, K. Williams, R. Barrès and N. Billestrup, *J. Biol. Chem.*, 2022, **298**, 102312.
3 L. Qi, Y. Wang, H. Wang and J. Deng, *Front. Immunol.*, 2020, **11**, 12.
4 M. Chen, Z. Chen, D. Huang, C. Sun, J. Xie, T. Chen, X. Zhao, Y. Huang, D. Li and B. Wu, *Pulm. Pharmacol. Ther.*, 2020, **65**, 102000.
5 A. Attiq, L. J. Yao, S. Afzal and M. A. Khan, *Int. Immunopharmacol.*, 2021, **101**, 108255.
6 Q. Ren, Y. Que, X. Min, W. Mu, D. Ruan, P. Wang, X. Dai, J. Cao, Y. Yang and G. Huang, *Arch. Pharm.*, 2025, **358**, e70137.
7 X. Liu, C. Zhao, H. Yang, J. Huang, Q. Zhou, Z. Zhang, X. Li, P. Yang and S. Hou, *Br. J. Ophthalmol.*, 2025, **3**, 326932.
8 M. Kong, Z. Xu, H. Lu, Y. Chen, Y. Zhang, X. Jiang and P. Wang, *J. Ethnopharmacol.*, 2026, **356**, 120785.
9 B. He, F. He, H. Li and L. Huang, *Sci. Adv.*, 2025, **15**, 38203.
10 L. Yue, X. Gao, W. Qi, L. Zhang and Y. Wang, *Nanoscale Horiz.*, 2026, **11**, 334–356.
11 Y. Chen, Z. Guo, J. Li, K. Wang and J. Huang, *Coord. Chem. Rev.*, 2025, **535**, 216673.
12 Y. Tang, J. Zou, Q. Li, Y. Liu, X. Guo, H. Bai, X. He, C. Gan, X. Zhao and W. Wu, *Int. J. Pharm.*, 2025, **684**, 126189.
13 E. Fang, X. Liu, M. Li, Z. Zhang, L. Song, B. Zhu, X. Wu, J. Liu, D. Zhao and Y. Li, *Signal Transduction Targeted Ther.*, 2022, **7**, 94.
14 X. Huang, C. Sun, H. Chen, C. Zhao and J. Lin, *Ther. Adv. Neurol. Disord.*, 2024, **17**, 17562864241273079.
15 D. Adams, A. Gonzalez-Duarte, W. D. O'Riordan, C.-C. Yang, M. Ueda, A. V. Kristen, I. Tournev, H. H. Schmidt, T. Coelho and J. L. Berk, *N. Engl. J. Med.*, 2018, **379**, 11–21.
16 S. Kotit, *Glob. Cardiol. Sci. Pract.*, 2023, **2023**, e202304.
17 Y. Sato, Y. Kinami, K. Hashiba and H. Harashima, *J. Controlled Release*, 2020, **322**, 217–226.
18 R. Chu, Y. Wang, J. Kong, T. Pan, Y. Yang and J. He, *J. Mater. Chem. B*, 2024, **12**, 4759–4784.
19 W. Zai, M. Yang, K. Jiang, J. Guan, H. Wang, K. Hu, C. Huang, J. Chen, W. Fu and C. Zhan, *Signal Transduction Targeted Ther.*, 2024, **9**, 150.
20 S. Sasikumar, A. Boden, S. Chameettachal, L. Cipolla, B. Cromer, P. Kingshott and F. Pati, *ACS Appl. Bio Mater.*, 2022, **5**, 3023–3037.
21 Q. Wang, Q. Jiang, D. Li, Z. Yang, L. Gao, F. Liu, C. Li, Y. Feng, Z. He and C. Luo, *Chin. Chem. Lett.*, 2024, **35**, 108683.
22 F. Rizvi, E. Everton, A. R. Smith, H. Liu, E. Osota, M. Beattie, Y. Tam, N. Pardi, D. Weissman and V. Gouon-Evans, *Nat. Commun.*, 2021, **12**, 613.
23 M. Kim, M. Jeong, S. Hur, Y. Cho, J. Park, H. Jung, Y. Seo, H. Woo, K. Nam and K. Lee, *Sci. Adv.*, 2021, **7**, eabf4398.
24 X. He, Z. Chang, F. Chen, W. Zhang, M. Sun, T. Shi, J. Liu, P. Chen, K. Zhang and S. Guan, *Acta Biomater.*, 2024, **174**, 281–296.
25 M. Huang, J. Liu, Y. Fan, J. Sun, J.-X. Cheng, X.-F. Zhang, B.-T. Zhai and D.-Y. Guo, *Int. J. Biol. Macromol.*, 2023, **253**, 127219.
26 Z. Liang, J. Li, S. Luo, S. Li, K. Zhao, H. Jiang, Y. Ou, J. Zhong, L. Luo and H. Huang, *RSC Adv.*, 2025, **15**, 19786–19801.
27 W. Ye, Q. Tang, T. Zhou, C. Zhou, C. Fan, X. Wang, C. Wang, K. Zhang, G. Liao and W. Zhou, *Eur. J. Med. Chem.*, 2024, **264**, 115988.
28 C. Zhang, Y. Teng, X. Bai, M. Tang, W. Stewart, J. J. Chen, X. Xu and X.-Q. Zhang, *ACS Nano*, 2024, **18**, 34375–34390.
29 J. Lu, Y. Dai, Y. He, T. Zhang, J. Zhang, X. Chen, C. Jiang and H. Lu, *J. Am. Chem. Soc.*, 2024, **146**, 3974–3983.
30 Y. Zhang, H. Liu, W. Zhen, T. Jiang and J. Cui, *Carbohydr. Res.*, 2025, **552**, 109426.

31 W. Ye, Q. Tang, T. Zhou, C. Zhou, C. Fan, X. Wang, C. Wang, K. Zhang, G. Liao and W. Zhou, *Eur. J. Med. Chem.*, 2024, **264**, 115988.
32 H. Nie, B. Qiu, Q.-X. Yang, Y. Zhao, X.-M. Liu, Y.-T. Zhang, F.-L. Liao and S.-Y. Zhang, *J. Liposome Res.*, 2021, **31**, 79–89.
33 L. J. Scott, *Drugs*, 2020, **80**, 335–339.
34 Y. Y. Syed, *Drugs*, 2023, **83**, 1729–1733.
35 S. J. Keam, *Drugs*, 2022, **82**, 1419–1425.
36 H. Nie, X.-M. Liu, Q.-X. Yang, X.-D. Luo, Y. Zhao and S.-Y. Zhang, *Int. J. Pharm.*, 2022, **624**, 121967.
37 Z.-X. Qin, L. Zuo, Z. Zeng, R. Ma, W. Xie, X. Zhu and X. Zhou, *Expert Opin. Drug Delivery*, 2025, **22**, 455–469.
38 J. Luo, Y. Jiang, X. Yin, W. Xue, J. Liu, M. Wang, S. Shi, Y. Pu and X. Li, *Int. J. Pharm.*, 2026, **693**, 126679.
39 A. Gabrielsen, Z. Feng, J. Fu, S. Ueckert, L. Egnell, J. Wikstrom, W. Wei, G. Chen, R. Friend and H. Zhan, *Eur. Heart J.*, 2024, **45**, ehae666.3327.
40 T. P. Prakash, A. E. Mullick, S. Riney, J. Yu, M. Nikan, C. Quirk, A. Crutchfield, S. S. Damle, S. Klein and E. E. Swayze, *Nucleic Acids Res.*, 2025, **53**, gkaf1063.

